

Estimating black hole masses in obscured AGN using X-rays

Mario Gliozzi¹★ and James K. Williams¹ and Dina A. Michel¹

¹ Department of Physics and Astronomy, George Mason University, 4400 University Drive, Fairfax, VA 22030

Accepted XXX. Received YYY; in original form ZZZ

ABSTRACT

Determining the black hole masses in active galactic nuclei (AGN) is of crucial importance to constrain the basic characteristics of their central engines and shed light on their growth and co-evolution with their host galaxies. While the black hole mass (M_{BH}) can be robustly measured with dynamical methods in bright type 1 AGN, where the variable primary emission and the broad line region (BLR) are directly observed, a direct measurement is considerably more challenging if not impossible for the vast majority of heavily obscured type 2 AGN. In this work, we tested the validity of an X-ray-based scaling method to constrain the M_{BH} in heavily absorbed AGN. To this end, we utilized a sample of type 2 AGN with good-quality hard X-ray data obtained by the *NuSTAR* satellite and with M_{BH} dynamically constrained from megamaser measurements. Our results indicate that, when the X-ray broadband spectra are fitted with physically motivated self-consistent models that properly account for absorption, scattering, and emission line contributions from the putative torus and constrain the primary X-ray emission, then the X-ray scaling method yields M_{BH} values that are consistent with those determined from megamaser measurements within their respective uncertainties. With this method we can therefore systematically determine the M_{BH} in any type 2 AGN, provided that they possess good-quality X-ray data and accrete at a moderate to high rate.

Key words: Galaxies: active – Galaxies: nuclei – X-rays: galaxies

1 INTRODUCTION

Historically, radio-quiet active galactic nuclei (AGN) have been divided into two main categories based on their optical spectroscopy: type 1 AGN, whose spectra are characterized by the presence of broad permitted lines (with full width at half maximum FWHM $> 2000 \text{ km s}^{-1}$) along with narrow forbidden lines, and type 2 AGN, where only narrow forbidden lines are detected (e.g., Khachikian & Weedman 1974; Antonucci 1983).

According to the basic AGN unification model, type 2 AGN can be considered as the obscured counterpart of type 1 AGN and their main differences can be simply ascribed to different viewing angles, due to the presence of an obscuring toroidal structure made of gas and dust surrounding the AGN (e.g., Osterbrock 1978; Antonucci 1993; Tadhunter 2008; Urry & Padovani 1995). However, over the years, theoretical and observational studies have revealed that the simplest version of the unification model, based on a smooth donut-shaped torus, is unable to explain several observations, favoring instead a scenario where the torus is clumpy, with a covering factor depending on various AGN properties, and where the overall obscuration occurs on different scales with significant contribution from the galaxy itself. See Netzer (2015) and Ramos Almeida & Ricci (2017) for recent comprehensive reviews on the unification model of AGN.

Regardless of the nature of the obscuration, in type 2 AGN, the central engine – an optical/UV emitting accretion disk, coupled with an X-ray emitting Comptonization corona – and the broad line region (BLR) are not directly accessible to observations. This makes it

more difficult to determine the properties of obscured AGN, which represent the majority of the AGN population and thus play a crucial role in our understanding of the AGN activity, census, and cosmological evolution (see Hickox & Alexander 2018 for a recent review on obscured AGN).

In order to shed light on the properties of the AGN central engine and its accretion state, we need to accurately determine the black hole mass (M_{BH}). In type 1 AGN, a reliable dynamical method frequently used is the so-called reverberation mapping method, where intrinsic changes in the continuum emission of the central engine, measured with some time delay in the line emission produced by the BLR, are used to constrain the M_{BH} , modulo a geometric factor (Blandford & McKee 1982; Peterson et al. 2004). On the other hand, in type 2 AGN, by definition the BLR is not visible and hence the reverberation mapping technique cannot be applied. Nevertheless, there is a small fraction of heavily obscured AGN for which it is still possible to measure the M_{BH} in a reliable way via a dynamical method. These are the sources that display water megamaser emission; if this emission is located in the accretion disk and is characterized by the Keplerian motion, then the M_{BH} can be constrained with great accuracy (e.g. Kuo et al. 2011).

In this work, we use a sample of heavily obscured type 2 AGN with M_{BH} constrained by megamaser measurements and with good-quality hard X-ray spectra obtained with the *Nuclear Spectroscopic Telescope Array* (*NuSTAR*), a focusing hard X-ray telescope launched in 2012 with large effective area and excellent sensitivity in the energy range 3–78 keV, where the signatures of absorption and reflection are most prominent. Our main goal is to test whether an X-ray scaling method that yields M_{BH} values broadly consistent with those ob-

★ E-mail: mgliozzi@gmu.edu

Table 1. Properties of the sample

Source name (1)	Distance (Mpc) (2)	M_{BH} ($10^6 M_{\odot}$) (3)	λ_{Edd} ($L_{\text{bol}}/L_{\text{Edd}}$) (4)	<i>NuSTAR</i> observation ID (5)	Exposure (ks) (6)
NGC 1068	14.4 ^a	8.0 ± 0.3	0.210 ± 0.053	60002033002	52.1
NGC 1194	53.2 ^b	65.0 ± 3.0	0.007 ± 0.002	60061035002	31.5
NGC 2273	25.7 ^b	7.5 ± 0.4	0.132 ± 0.034	60001064002	23.2
NGC 3079	17.3 ^c	$2.4^{+2.4}_{-1.2}$	0.011 ± 0.009	60061097002	21.5
NGC 3393	50.0 ^d	31.0 ± 2.0	0.062 ± 0.016	60061205002	15.7
NGC 4388	19.0 ^b	8.5 ± 0.2	0.035 ± 0.009	60061228002	21.4
NGC 4945	3.7 ^e	1.4 ± 0.7	0.135 ± 0.075	60002051004	54.6
IC 2560	26.0 ^f	3.5 ± 0.5	0.175 ± 0.050	50001039004	49.6
Circinus	4.2 ^g	1.7 ± 0.3	0.143 ± 0.044	60002039002	53.9

Columns: 1 = megamaser AGN name. 2 = distance used computing the M_{BH} from the maser measurements. References for the distances and black hole masses are (a) [Lodato & Bertin \(2003\)](#), (b) [Kuo et al. \(2011\)](#), (c) [Kondratko, Greenhill, & Moran \(2005\)](#), (d) [Kondratko, Greenhill, & Moran \(2008\)](#), (e) [Greenhill et al. \(1997\)](#), (f) [Yamauchi et al. \(2012\)](#), and (g) [Greenhill et al. \(2003\)](#). 3 = black hole mass. 4 = Eddington ratio with Brightman’s bolometric correction of $10\times$ to L_X from [Brightman et al. \(2016\)](#). 5 = *NuSTAR* observation ID. 6 = exposure time.

tained from reverberation mapping in type 1 AGN can be extended to type 2 AGN.

The paper is structured as follows. In Section 2, we describe the sample properties and the X-ray data reduction. In Section 3, we report on the spectral analysis of *NuSTAR* data. The application of the X-ray scaling method and the comparison between the M_{BH} values derived with this method and those obtained from megamaser measurements are described in Section 4. We discuss the main results and draw our conclusions in Section 5.

2 SAMPLE SELECTION AND DATA REDUCTION

We chose our sample of type 2 AGN based on the following two criteria: these objects must have 1) the M_{BH} dynamically determined by megamaser disk measurements, and 2) good-quality hard X-ray data. The former criterion is crucial to quantitatively test the validity of the X-ray scaling method applied to heavily obscured AGN, whereas the latter criterion is necessary to robustly constrain the properties of the primary X-ray emission by accurately assessing the contributions of absorption and reflection caused by the putative torus. These criteria are fulfilled by the sample described by [Brightman et al. \(2016\)](#), which is largely based on the sample of megamasers analyzed by [Masini et al. \(2016\)](#) and spans a range in X-ray luminosity between 10^{42} erg s^{−1} and a few units in 10^{43} erg s^{−1}. The general properties of this sample, including the distance used to determine the M_{BH} from maser measurements, the M_{BH} itself, and the Eddington ratio $\lambda_{\text{Edd}} = L_{\text{bol}}/L_{\text{Edd}}$, are reported in Table 1.

The archival *NuSTAR* data of these nine objects were calibrated and screened using the *NuSTAR* data analysis pipeline `nupipeline` with standard filtering criteria and the calibration database CALDB version 20191219. From the calibrated and screened event files we extracted light curves and spectra, along with the RMF and ARF files necessary for the spectral analysis, using the `nuproduct` script. The extraction regions used for both focal plane modules, FPMA and FPMB, are circular regions of radii ranging from 40'' to 100'' depending on the brightness of the source, and centered on the brightest centroid. Background spectra and light curves were extracted by placing circles of the same size used for the source in source-free regions of the same detector. No flares were found in the background light curves. All

spectra were binned with a minimum of 20 counts per bin using the HEASoft task `grppha` 3.0.1 for the χ^2 statistics to be valid.

3 SPECTRAL ANALYSIS

The X-ray spectral analysis was performed using the `xSPEC v. 12.9.0` software package ([Arnaud 1996](#)), and the errors quoted on the spectral parameters represent the 1σ confidence level.

The *NuSTAR* spectra of this sample have already been reasonably well fitted with self-consistent physically motivated models such as MYTorus ([Murphy & Yaqoob 2009](#)) and Torus ([Brightman & Nandra 2011](#)) to account for the continuum scattering and absorption, as well as the fluorescent line emission produced by the torus, whereas the primary emission was parametrized with a phenomenological power-law model. However, in order to apply the X-ray scaling method (whose key features are described in the following section), the primary emission needs to be parametrized by the Bulk Motion Comptonization model (BMC), which is a generic Comptonization model that convolves thermal seed photons producing a power law ([Titarchuk, Mastichiadis, & Kylafis 1997](#)). This model, which can be used to parametrize both the bulk motion and the thermal Comptonization, is described by four spectral parameters: the normalization N_{BMC} , the spectral index α , the temperature of the seed photons kT , and $\log A$, where A is related to the fraction of scattered seed photons f by the relationship $A = (f + 1)/f$. Unlike the phenomenological power-law model, the BMC parameters are computed in a self-consistent way, and the power-law component produced by the BMC does not extend to arbitrarily low energies.

We carried out a homogeneous systematic reanalysis of the *NuSTAR* spectra of these sources. We started from the best-fit models reported in the literature but utilized the Borus model ([Baloković et al. 2018](#)), which can be considered as an evolution of the previous torus models. Specifically, Borus has the same geometry implemented in Torus but can also be used in a decoupled mode, where the column density N_{H} responsible for the continuum scattering and fluorescent line emission is allowed to be different from the N_{H} responsible for the attenuation of the primary component. Additionally, unlike Torus, this model correctly accounts for the absorption experienced by the photons backscattered from the far side of the inner

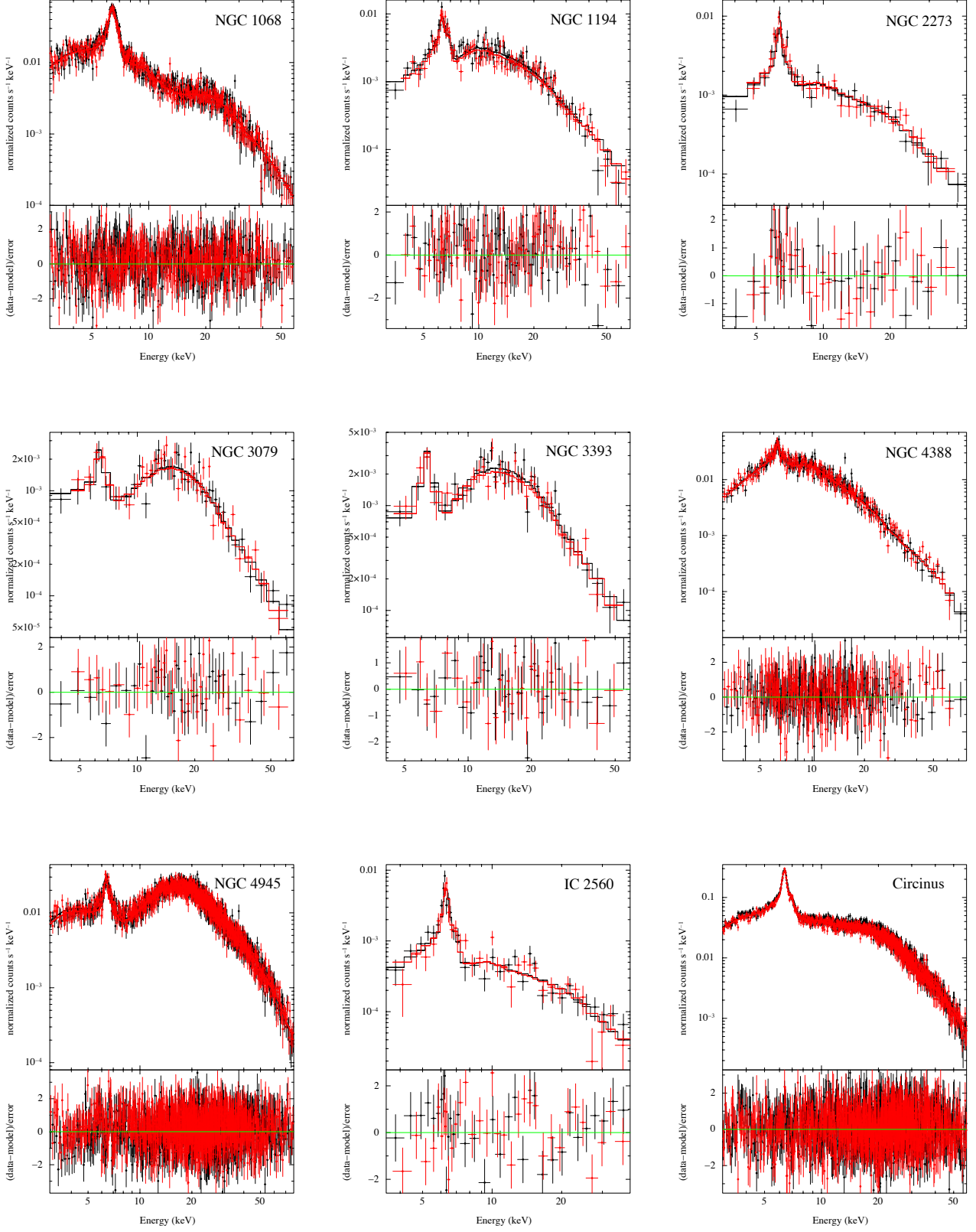


Figure 1. The top panels show the *NuSTAR* spectra (black data points indicate FPMA data whereas the red ones indicate FPMB data) with the best-fit models, whereas the bottom panels show the data-to-model ratios.

Table 2. Spectral Results

Source name (1)	N_{HGal} (10^{20} cm^{-2}) (2)	$\log(N_{\text{Hbor}})$ (3)	$\cos \theta$ (4)	CFtor (%) (5)	A_{Fe} (6)	N_{Hmytz} (10^{24} cm^{-2}) (7)	Γ (8)	N_{BMC} (9)	$\log A$ (10)	f_s (%) (11)	(χ^2/dof) (12)
NGC 1068	2.59	23.3 ± 0.1	0.1	15	1.0	3.5 ± 0.1	$1.98^{+0.01}_{-0.01}$	$2.2^{+0.1}_{-0.1} \times 10^{-3}$	0.08	1.6	754.9/713
NGC 1194	5.53	23.9 ± 0.1	0.1	91	3.2	0.8 ± 0.1	$1.62^{+0.05}_{-0.05}$	$6.4^{+1.1}_{-0.8} \times 10^{-5}$	0.57	4.0	194.3/167
NGC 2273	5.80	25.0 ± 0.7	0.1	15	1.0	6.8 ± 0.4	$1.95^{+0.05}_{-0.05}$	$3.1^{+0.2}_{-0.2} \times 10^{-3}$	2.0	...	54.0/57
NGC 3079	0.87	24.5 ± 0.1	0.1	20	1.0	2.9 ± 0.1	$1.91^{+0.05}_{-0.06}$	$1.1^{+0.2}_{-0.2} \times 10^{-3}$	0.8	0.3	80.1/75
NGC 3393	6.13	25.2 ± 0.2	0.1	15	1.0	2.4 ± 0.1	$1.86^{+0.10}_{-0.10}$	$9.6^{+3.1}_{-1.2} \times 10^{-4}$	0.22	...	54.3/65
NGC 4388	2.57	23.6 ± 0.1	0.1	91	1.0	0.4 ± 0.1	$1.66^{+0.04}_{-0.04}$	$3.3^{+0.5}_{-0.4} \times 10^{-4}$	-0.55	17.0	435.2/420
NGC 4945	14.0	24.4 ± 0.1	0.1	91	0.8	3.0 ± 0.7	$1.74^{+0.05}_{-0.05}$	$1.6^{+0.1}_{-0.1} \times 10^{-3}$	2.15	0.5	1699.8/1716
IC 2560	6.51	25.1 ± 0.1	0.1	15	2.3	6.9 ± 0.1	$2.08^{+0.08}_{-0.08}$	$1.8^{+0.4}_{-0.3} \times 10^{-3}$	2.0	...	88.3/64
Circinus	52.5	23.6 ± 0.1	0.1	24	1.7	1.6 ± 0.1	$2.17^{+0.01}_{-0.01}$	$9.8^{+0.1}_{-0.2} \times 10^{-3}$	-0.43	3.3	1713.2/1714

Columns: 1 = megamaser AGN name. 2 = Galactic column density from NASA's HEASARC. 3 = column density calculated with the *Borus* model. 4 = cosine of the inclination angle. 5 = covering factor. 6 = iron abundance relative to the solar value. 7 = column density calculated with the *MYTorus* model. 8 = photon index. 9 = normalization of the BMC model. 10 = logarithm of A , where $A = (f + 1)/f$ and f is the fraction of seed photons that are scattered. 11 = fraction of the primary emission scattered along the line of sight by an extended ionized reflector. 12 = χ^2 divided by degrees of freedom.

torus. With respect to *MYTorus*, *Borus* contains additional emission lines, has a larger range for N_{H} , and directly yields the value of the covering fraction. However, since *Borus* only parametrizes the scattered continuum and the fluorescent line components associated with the torus, to account for the absorption and scattering experienced by the primary emission, we utilized the zeroth-order component of *MYTorus* (*MYTZ*), which properly includes the effects of the Klein-Nishina Compton scattering cross section that are relevant in heavily absorbed AGN at energies above 10 keV. In summary, our procedure can be summarized in three steps: 1) we started from the spectral best fits reported in the literature; 2) we then substituted *Borus* (more specifically, we used the `borus02_v170323a.fits` table) for either *Torus* or *MYTorus* to account for the scattered and line components, and used the zeroth-order component of *MYTorus* for the transmitted one; 3) finally, we substituted BMC for the power-law model used for the primary emission.

In the spectral fitting, in order to preserve the self-consistency of these physically motivated torus models, which are created by Monte Carlo simulations using a power law to parametrize the X-ray primary emission, one needs to link the primary emission parameters – the photon index Γ and the normalization N_{PL} – to the input parameters of the scattered continuum and emission-line components. In the case of the BMC model, the power-law slope is described by the spectral index α , which is related to the photon index by the relationship $\Gamma = \alpha + 1$. However, there is not a known mathematical equation linking the normalizations N_{BMC} and N_{PL} . We therefore derived this relationship empirically by using a sample of clean type 1 AGN (i.e., AGN without cold or warm absorbers), whose details are described in [Williams, Glozzi, & Rudzinsky \(2018\)](#); [Glozzi & Williams \(2020\)](#). We fitted the 2–10 keV *XMM-Newton* spectra twice, first with the BMC model and then with a power law. The results of this analysis are illustrated in Fig. 2, where $N_{\text{PL}}/N_{\text{BMC}}$ is plotted versus N_{BMC} , showing that, regardless of the value of N_{BMC} , the normalization ratios cluster around the average value, 30.8 ± 0.9 , represented by the longer-dashed line, with moderate scattering of $\sigma = 7.2$, represented by the shorter-dashed lines. Fig. 2, where the data point's size and color provide information about the photon index, also reveals a tendency for the AGN with steeper spectra to have larger values of $N_{\text{PL}}/N_{\text{BMC}}$. This trend is formally confirmed by a least-squares best

fit of $N_{\text{PL}}/N_{\text{BMC}}$ vs. Γ , which yields $N_{\text{PL}}/N_{\text{BMC}} = -18.9 + 26.3\Gamma$, with a Pearson's correlation coefficient of 0.85.

These results are in agreement with those obtained from a series of simulations carried out with the `fakeit` command in *XSPEC*. Simulating spectra of the BMC model with the parameters varying over a broad range, and then fitting them with a power-law model, we found that $N_{\text{PL}}/N_{\text{BMC}}$ shows a horizontal trend when plotted vs. N_{BMC} with an average value consistent with 30 for $\Gamma = 1.9$, whereas the horizontal trend is consistent with an average value of 24 for $\Gamma = 1.6$ and 33 for $\Gamma = 2.2$.

Based on these findings, in our spectral fitting of the megamaser sample we forced N_{BMC} to be equal to $N_{\text{PL}}/30$ by linking these parameters to reflect this relationship. For completeness, and to take into account the weak dependence of $N_{\text{PL}}/N_{\text{BMC}}$ on Γ , we have also carried out the spectral analysis assuming $N_{\text{PL}}/N_{\text{BMC}} = 24$ (i.e., the average value minus one standard deviation) for flat spectrum sources and $N_{\text{PL}}/N_{\text{BMC}} = 38$ (average + σ) for steep spectrum sources.

We note that, compared to Γ and N_{BMC} , the remaining BMC parameters kT and $\log A$ play a marginal role in the shape of the spectrum and in the determination of the M_{BH} , as explicitly assessed in [Glozzi et al. \(2011\)](#). Therefore, to limit the number of free parameters, we fixed kT to 0.1 keV, which is consistent with the values generally obtained when the BMC model is fitted to X-ray AGN spectra (e.g., [Glozzi et al. 2011](#); [Williams, Glozzi, & Rudzinsky 2018](#)), whereas $\log A$ was fixed to the best-fit value obtained in the first fitting iteration.

Our baseline model for all type 2 AGN fitted in this work is expressed in the *XSPEC* syntax as follows:

`phabs * (atable(Borus) + MYTZ * BMC + const * BMC)`

where the first absorption model `phabs` accounts for our Galaxy contribution, the *Borus* table model parametrizes the continuum scattering and fluorescent emission line components associated with the torus, and *MYTZ* models the absorption and Compton scattering acting on the transmitted primary emission, which is described by the Comptonization model BMC. The last additive component `const*BMC` parametrizes the fraction of primary emission directly scattered towards the observer by a putative optically thin ionized

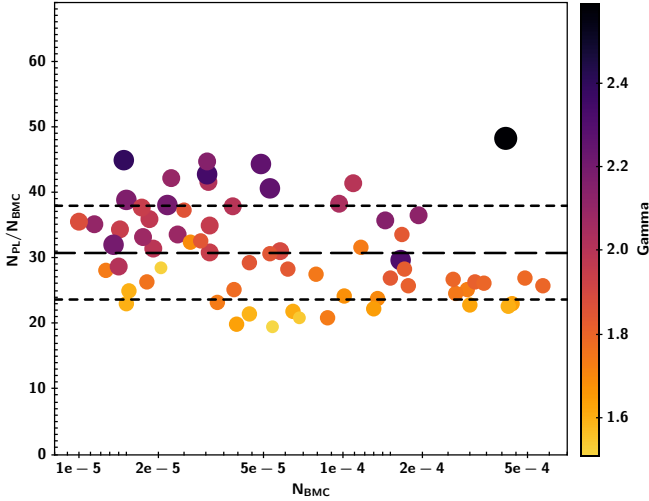


Figure 2. $N_{\text{PL}}/N_{\text{BMC}}$ plotted vs. N_{BMC} for a sample of “clean” type 1 AGN (i.e., AGN with negligible warm or cold absorbers). The black longer-dashed line represents the average value, whereas the shorter-dashed lines indicate the one standard deviation levels from the average. Both the data point’s size and color provide information on the source’s photon index Γ : the larger the symbol and the darker the color, the steeper the Γ .

medium, which is often observed below 5 keV in spectra of heavily obscured AGN (e.g., [Yaqoob 2012](#)).

Depending on the source and the complexity of its X-ray spectrum, additional components (such as the host galaxy contribution, individual lines, additional absorption and scattering components, or models describing off-nuclear sources contained in the *NuSTAR* extraction region) are included and described in the individual notes of each source reported in the Appendix.

The spectral parameters obtained by fitting this baseline model are reported in Table 2, and the best fits and model-to-data ratios are shown in Fig 1.

4 BLACK HOLE MASSES

4.1 M_{BH} from the X-ray scaling method

The X-ray scaling method was first introduced by [Shaposhnikov & Titarchuk \(2009\)](#), who showed that the BH mass and distance D of any stellar mass BH can be obtained by scaling these properties from those of an appropriate reference source (i.e., a BH system with M_{BH} dynamically determined and distance tightly constrained). In its original form this technique exploits the similarity of the trends displayed by different BH systems in two plots – the photon index Γ vs. quasi-periodic oscillation (QPO) frequency plot and the $N_{\text{BMC}}-\Gamma$ diagram – to derive their M_{BH} and D .

Based on the assumption that the process leading to the ubiquitous emission of X-rays – the Comptonization of seed photons produced by the accretion disk – is the same in all BH systems regardless of their mass, this method can in principle be extended to any BH including the supermassive BHs at the cores of AGN. In the latter case, since the detection of QPOs is extremely rare but the distance is generally well constrained by redshift or Cepheid measurements, only the $N_{\text{BMC}}-\Gamma$ diagram is used to determine the M_{BH} . Indeed, over the years, this method has been successfully applied to stellar mass BHs (e.g., [Seifina, Titarchuk, & Shaposhnikov 2014](#); [Titarchuk](#)

& [Seifina 2016](#)) and to ultraluminous X-ray sources (e.g., [Titarchuk & Seifina 2016](#); [Jang et al. 2018](#)), as well as to a handful of AGN that showed high spectral and temporal variability during deep X-ray exposures (e.g., [Gliozzi et al. 2010](#); [Giacché, Gilli, & Titarchuk 2014](#); [Seifina, Chekhtman, & Titarchuk 2018](#).)

Although the vast majority of AGN do not possess long-term X-ray observations and do not show strong intrinsic spectral variability (i.e., variability described by substantial changes of Γ not caused by obscuration events), the X-ray scaling method can be extended to any type 1 AGN with one good-quality X-ray observation. Indeed, [Gliozzi et al. \(2011\)](#) demonstrated that the M_{BH} values determined with this method are fully consistent with the corresponding values obtained from the reverberation mapping technique. The reference sources, used in that study and then also in this work, are three stellar mass BHs residing in X-ray binaries – GRO J1655-40, GX 339-4, and XTE J1550-564 – with M_{BH} dynamically determined and spectral evolution during the rising and decaying phases of their outbursts mathematically parametrized by [Shaposhnikov & Titarchuk \(2009\)](#). The physical properties of the stellar references and the mathematical description of their spectral trends, as well as the details of the method, are reported in [Gliozzi et al. \(2011\)](#).

In summary, all the reference trends yielded M_{BH} measurements consistent with the reverberation mapping values within their nominal uncertainties, with the decaying trends showing a slightly better agreement than the rising trends, which have a tendency to underestimate M_{BH} to a moderate degree. Unfortunately, the most reliable reference source – GRO J1655-40 during the 2005 decaying phase (hereafter GROD05) – has a fairly small range of Γ during its spectral transition limiting its application to sources with relatively flat photon indices. Using the reverberation mapping values as calibration, it was determined that for AGN with steep spectra ($\Gamma > 2$) the best estimate of M_{BH} is obtained using the value derived from the rising phase of the 1998 outburst of XTE J1550-564 multiplied by a factor of 3 (hereafter 3*XTER98). Below, we summarize the general principles at the base of this technique; a more detailed explanation can be found in [Shaposhnikov & Titarchuk \(2009\)](#) and [Gliozzi et al. \(2011\)](#). For completeness, in the Appendix we report the basic information on the reference sources, including the mathematical expression of their spectral trends, which is necessary to derive M_{BH} using the equation reported below.

The scaling method assumes that all BH systems accreting at a moderate or high rate undergo similar spectral transitions, characterized by the “softer when brighter” trend (i.e., the X-ray spectrum softens when the accretion and hence the luminosity increases). These spectral transitions are routinely observed in stellar BHs (e.g., [Remillard & McClintock 2006](#)) and often found in samples of AGN (e.g., [Shemmer et al. 2008](#); [Risaliti, Young, & Elvis 2009](#); [Brightman et al. 2013, 2016](#)), which are characterized by considerably longer dynamical timescales, making it nearly impossible to witness a genuine state transition in a supermassive BH system, although a few long monitoring studies have observed this spectral trend in individual AGN (e.g., [Sobolewska & Papadakis 2009](#)). The “softer when brighter” trend, usually illustrated by plotting the photon index versus the Eddington ratio λ_{Edd} , is seen with some scattering in numerous type 1 AGN samples and also in the heavily absorbed type 2 AGN, which are the focus of our work ([Brightman et al. 2016](#)). This lends support to the hypothesis that the photon index Γ is a reliable indicator of the accretion state of any BH.

Indeed, this is the fundamental assumption of the X-ray scaling method: Γ is indicative of the accretion state of the source, and BH systems in the same accretion state are characterized by the same accretion rate (in Eddington units) and the same radiative efficiency

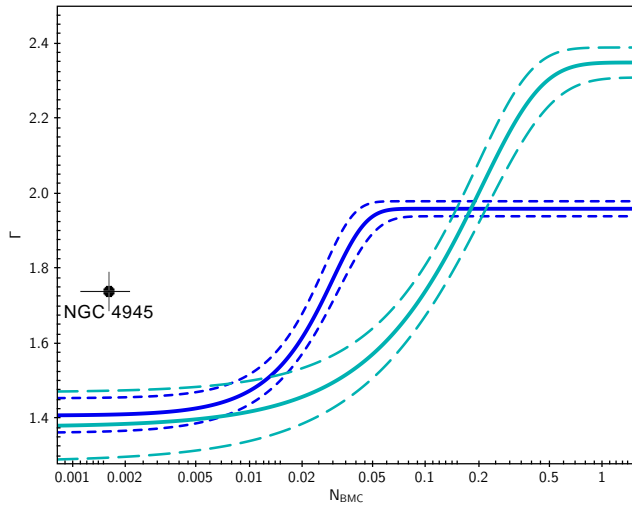


Figure 3. $N_{\text{BMC}}-\Gamma$ plot, showing the data point corresponding to NGC 4945 and two reference patterns; the darker trend refers to GROD05, the spectral evolution of GRO 1655-40 during the decay of an outburst that occurred in 2005, and the lighter color trend indicates GROR05, the spectral evolution shown by the same source during the outburst rise. The dashed lines indicate the uncertainties in the reference spectral trends, whereas the error bars represent the uncertainties of the AGN spectral parameters.

η . As a consequence, when we compare the accretion luminosity ($L \propto \eta M_{\text{BH}} \dot{m}$) in BH systems that are in the same accretion state (i.e., with the same Γ), we are directly comparing their M_{BH} . This explains why the comparison of the values of the normalization of the BMC model, N_{BMC} (which is defined as the accretion luminosity in units of $10^{39} \text{ erg s}^{-1}$ divided by the distance squared in units of 10 kpc), computed at the same value of Γ between the AGN and a known stellar BH reference source, yields the M_{BH} . This is illustrated in Fig. 3 and mathematically described by

$$M_{\text{BH,AGN}} = M_{\text{BH,ref}} \times \left(\frac{N_{\text{BMC,AGN}}}{N_{\text{BMC,ref}}} \right) \times \left(\frac{d_{\text{AGN}}^2}{d_{\text{ref}}^2} \right)$$

where $N_{\text{BMC,ref}}$ and d_{ref} are the BMC model normalization and distance of the stellar mass BH system used as a reference.

Fig. 3 illustrates the X-ray scaling method and its inherent uncertainties that are related to the statistical errors on the spectral parameters Γ and N_{BMC} and on the uncertainty of the reference source spectral trend (shown by the dashed lines), as well as on the specific reference source trend utilized. Although similar in shape, the reference spectral trends show some differences (e.g., in their plateau levels and slopes), leading to slightly different M_{BH} values. From Fig. 3, it is clear that these differences exist also between the rise and decay phases of the same reference source.

It is important to note that at very low accretion rates both stellar mass and supermassive BHs show an anti-correlation between Γ and λ_{Edd} (e.g., Constantin et al. 2009; Gu & Cao 2009; Gültekin et al. 2012). Since the X-ray scaling method is based on the positive correlation between these two quantities, it cannot be applied to determine the M_{BH} of objects in the very low-accretion regime. This was explicitly demonstrated by the work of Jang et al. (2014), who analyzed a sample of low-luminosity low-accreting AGN.

In the following, we systematically estimate the M_{BH} using all the reference sources available (depending on the AGN's Γ , not all reference sources can be used since their photon index ranges vary from reference source to reference source) and then compute the M_{BH}

average value and its uncertainty σ/\sqrt{n} (where σ is the standard deviation and n is the number of reference trends utilized). As already explained above, for AGN with steep spectra, the most reliable estimate of M_{BH} is obtained using the 3*XTER98 reference trend; therefore, we also include this value in Table 3. All M_{BH} values listed in this table were computed assuming $N_{\text{PL}}/N_{\text{BMC}} = 30$; however, for completeness, we also report the M_{BH} obtained assuming $N_{\text{PL}}/N_{\text{BMC}} = 24$ and 38 for flat- and steep-spectrum sources, respectively. We note that such changes in $N_{\text{PL}}/N_{\text{BMC}}$ lead to M_{BH} values that are consistent with the values obtained with the original assumption $N_{\text{PL}}/N_{\text{BMC}} = 30$, within the respective M_{BH} uncertainties that are of the order of 10%–40%.

The M_{BH} values obtained with the different reference sources and their average are illustrated in Fig. 4. As already found in Glozzi et al. (2011) for the reverberation mapping AGN sample, the reference trends of decaying outbursts yield systematically larger M_{BH} values compared to those obtained from the rising trends. For each obscured AGN, several M_{BH} values obtained from different reference sources and their average appear to be broadly consistent with the value obtained from megamaser measurements (a quantitative comparison is carried out in the next subsection). The only noticeable exception is NGC 1194, for which the X-ray scaling method yields values significantly lower than the maser one. This discrepancy however is not surprising, since this source has a fairly low accretion rate and in that regime the X-ray scaling method cannot be safely applied.

4.2 Black hole mass comparison

To compare the M_{BH} values obtained from the X-ray scaling method with the maser ones in a quantitative way, we computed, using all the available reference trends, the difference $\Delta M_{\text{BH}} = M_{\text{BH,maser}} - M_{\text{BH,scaling}}$ and its uncertainty σ_{diff} , obtained by adding the respective errors in quadrature. As explained before, the error on the M_{BH} inferred from the scaling method includes the uncertainties on the spectral AGN parameters and on the reference trends in the $N_{\text{BMC}}-\Gamma$ diagram. Depending on the reference trend utilized, the percentage uncertainties range from 10%–15% for GROD05 and GXD03 to 30%–40% for XTER98, which is also the percentage uncertainty of the average M_{BH} .

The error on the M_{BH} obtained with megamaser measurements accounts for the uncertainties associated with the source position and with the fitting of the Keplerian rotation curve (Kuo et al. 2011). For the uncertainties on the M_{BH} determined via megamaser measurements we used the errors quoted in the literature with the exception of NGC 4388, for which we multiplied the quoted uncertainty by a factor of 10; this yields a percentage error of $\sim 24\%$, which better reflects the actual uncertainty on the M_{BH} in this source, where there is no systemic maser detected and the five maser spots detected are not sufficient to demonstrate that the rotation is Keplerian (Kuo et al. 2011). Note that both methods explicitly depend on the sources' distances and hence, in principle, their total uncertainties should account also for the distance uncertainties (indeed some of the sources of this maser sample are fairly close and thus their distances cannot be obtained from the redshift and Hubble's law). However, since our goal is to compare the two methods, we can avoid the uncertainty associated with the distance by assuming the exact same distance used in the maser papers.

We used the criterion $\Delta M_{\text{BH}}/\sigma_{\text{diff}} < 3$ to assess whether the M_{BH} values derived with these two methods are statistically consistent. In other words, the X-ray scaling measurements of the M_{BH} are considered formally consistent with the corresponding megamaser values if their difference is less than three times the uncertainty σ_{diff} .

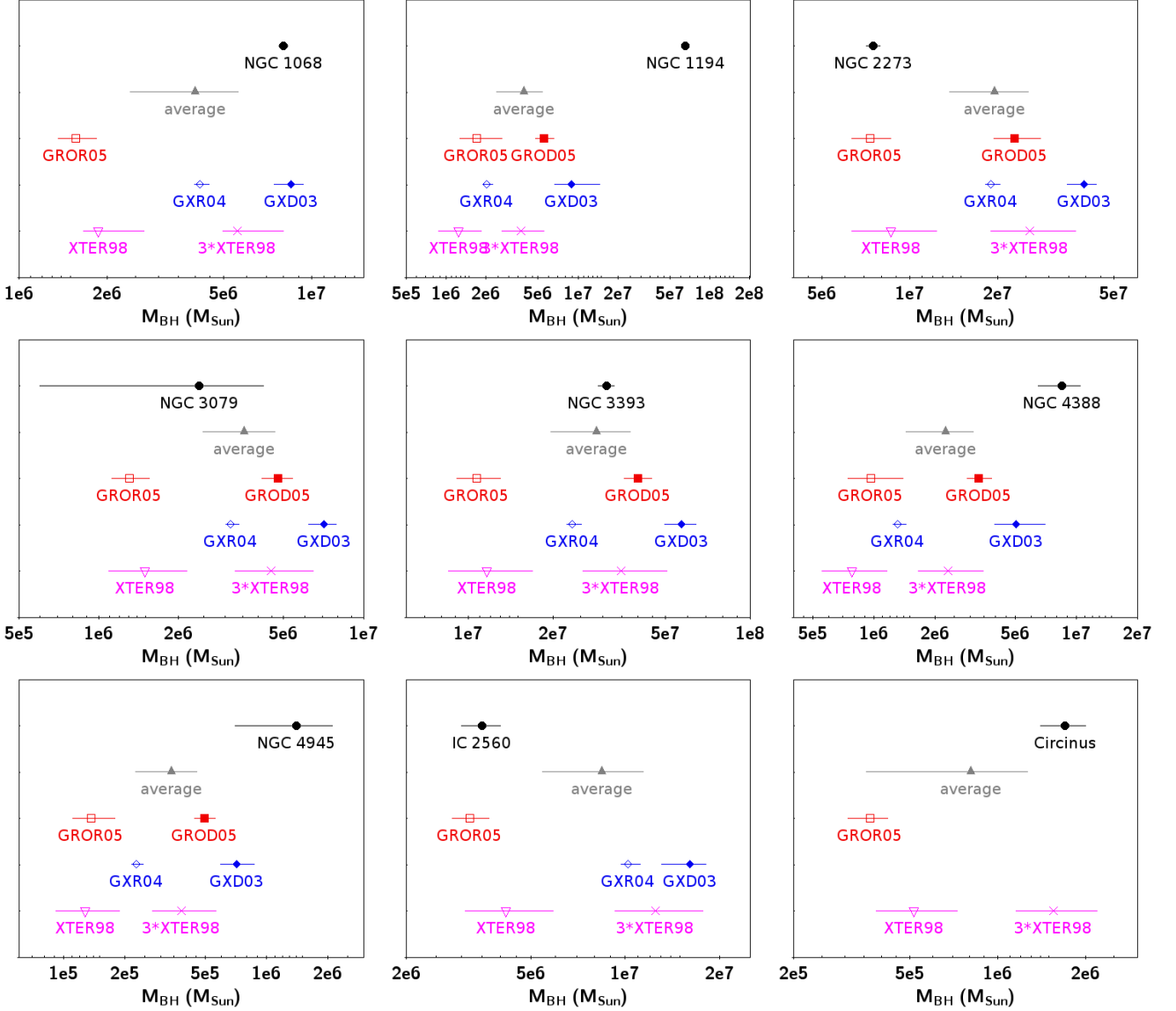


Figure 4. M_{BH} values obtained with the X-ray scaling method using different reference sources, compared with M_{BH} obtained from megamaser measurements, which are represented by the black symbols at the top of each panel.

The results of these comparisons are summarized in Table 4 and illustrated in Fig. 5, where the dashed lines represent the 3σ levels. From this figure it is evident that every source has at least one M_{BH} scaling value that is consistent with the maser one, with GROD05 and GXD03 being the most reliable ones, along with the average M_{BH} and the value obtained with $3 \times \text{XTER98}$. The latter ones are always within 3σ from the megamaser value, also by virtue of their slightly larger uncertainties.

An alternative way to compare the two methods is offered by the ratio $M_{\text{BH,maser}}/M_{\text{BH,scaling}}$. The ratios, obtained by dividing the megamaser M_{BH} by each of the available reference sources, as well as by the M_{BH} average and by $3 \times \text{XTER98}$, are reported in Table 5 and illustrated in Fig. 6, where the M_{BH} values obtained with the scaling method for the most reliable references (GROD05, GXD03, $3 \times \text{XTER98}$) and the average values are plotted versus their respective megamaser values. From this figure, one can see that, for GROD05 (top left panel), $3 \times \text{XTER98}$ (bottom left panel), and the average (bottom right panel), all values are consistent with the ratio of 1

within a factor of 3, and a good agreement is found also with GXD03 (top right panel) with two sources (IC 2560 and NGC 2273) that have slightly larger values.

Based on the values reported in Table 5, all ratios obtained from these reference trends are consistent with unity at the 3σ limit (i.e., their ratio $\pm 3\sigma$ is consistent with 1) confirming the statistical agreement between the two methods. Finally, we note that using $N_{\text{PL}}/N_{\text{BMC}} = 24$ (for flat spectrum sources) and 38 (for steep spectrum sources) confirms and reinforces the conclusions derived from the original assumption $N_{\text{PL}}/N_{\text{BMC}} = 30$.

5 DISCUSSION AND CONCLUSIONS

Constraining the M_{BH} in AGN is of crucial importance, since it determines the space and temporal scales of BHs, constrains their accretion rate via the Eddington ratio, and plays an essential role in our understanding of the BH growth and co-evolution with the

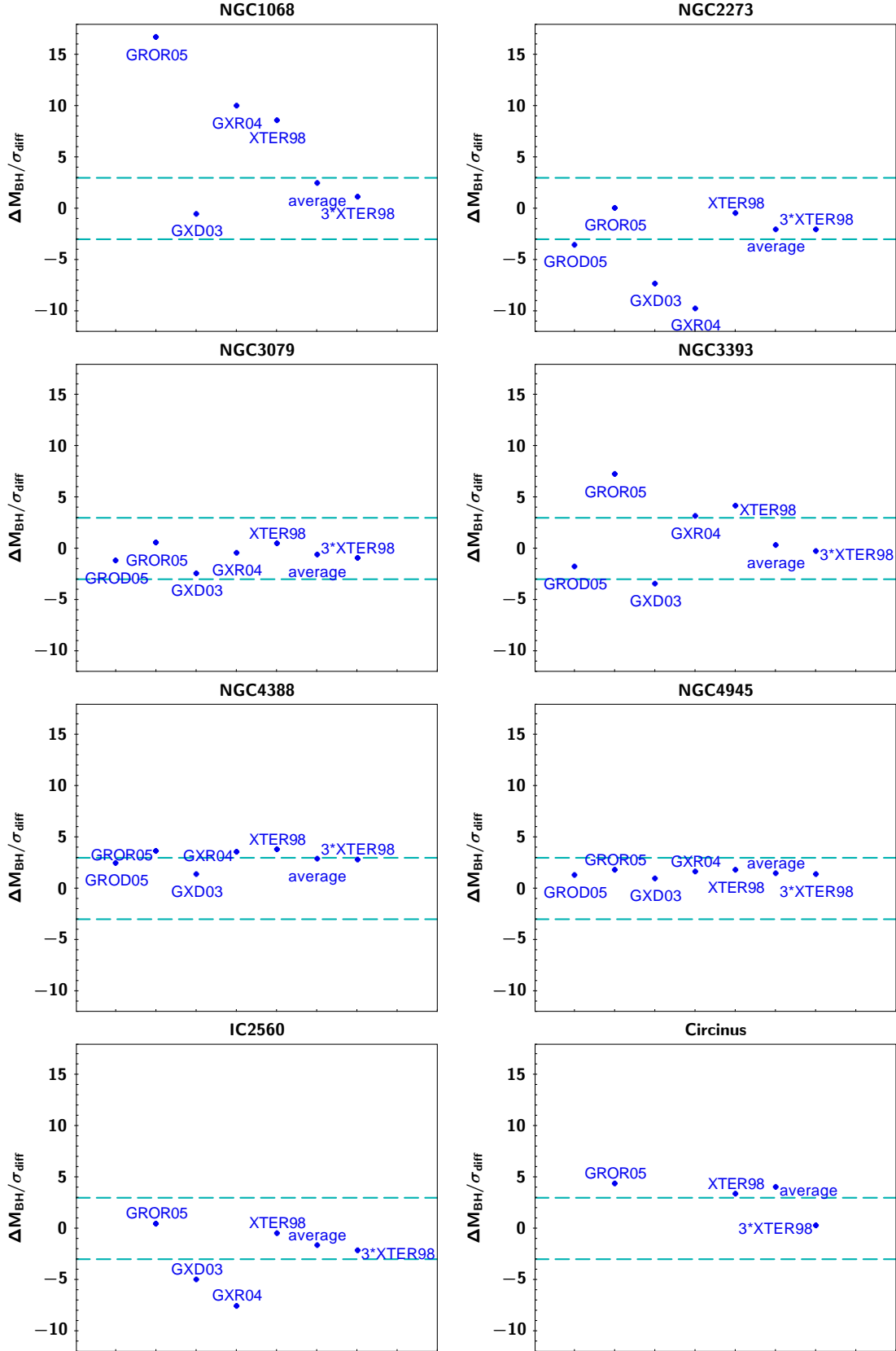


Figure 5. Plots showing the difference between the BH mass determined from megamaser measurements and the values obtained with the X-ray scaling method for the different reference sources, divided by the uncertainty of the difference, $\Delta M_{\text{BH}}/\sigma_{\text{diff}}$. The horizontal dashed lines enclose the region where the difference between the BH masses is within 3σ .

Table 3. Black hole masses with the X-ray scaling method

Source name (1)	$M_{\text{BH,GROD05}}$ ($10^6 M_{\odot}$) (2)	$M_{\text{BH,GROR05}}$ ($10^6 M_{\odot}$) (3)	$M_{\text{BH,GXD03}}$ ($10^6 M_{\odot}$) (4)	$M_{\text{BH,GXR04}}$ ($10^6 M_{\odot}$) (5)	$M_{\text{BH,XTER98}}$ ($10^6 M_{\odot}$) (6)	$M_{\text{BH,aver}}$ ($10^6 M_{\odot}$) (7)	$M_{\text{BH},3*\text{XTER98}}$ ($10^6 M_{\odot}$) (8)
NGC 1068	...	$1.6^{+0.3}_{-0.2}$	$8.5^{+0.8}_{-1.0}$	$4.1^{+0.3}_{-0.2}$	$1.9^{+0.8}_{-0.5}$	$4.0^{+1.6}_{-1.6}$	$5.6^{+2.4}_{-1.5}$
NGC 1194	$5.6^{+1.0}_{-0.7}$	$1.7^{+1.0}_{-0.4}$	$9.0^{+5.7}_{-2.3}$	$2.0^{+0.2}_{-0.1}$	$1.2^{+0.6}_{-0.4}$	$3.9^{+1.5}_{-1.5}$	$3.7^{+1.9}_{-1.1}$
$N_{\text{PL}}/N_{\text{BMC}} = 24$	$6.9^{+1.5}_{-1.0}$	$2.2^{+1.6}_{-0.6}$	$12^{+13}_{-3.5}$	$2.4^{+0.4}_{-0.1}$	$1.5^{+0.7}_{-0.4}$	$5.0^{+2.0}_{-2.0}$	$4.4^{+2.2}_{-1.3}$
NGC 2273	$22.8^{+5.2}_{-3.4}$	$7.3^{+1.3}_{-1.0}$	$39.6^{+4.0}_{-4.8}$	$19.0^{+1.4}_{-0.8}$	$8.6^{+3.8}_{-2.3}$	$19.5^{+5.8}_{-5.8}$	$25.8^{+11.3}_{-6.9}$
NGC 3079	$4.8^{+0.6}_{-0.6}$	$1.3^{+0.3}_{-0.2}$	$7.1^{+0.8}_{-0.9}$	$3.2^{+0.2}_{-0.1}$	$1.5^{+0.7}_{-0.4}$	$3.6^{+1.1}_{-1.1}$	$4.5^{+2.0}_{-1.2}$
NGC 3393	$40.1^{+4.8}_{-4.2}$	$10.7^{+2.3}_{-1.6}$	$57.1^{+7.3}_{-7.5}$	$23.3^{+1.8}_{-1.0}$	$11.6^{+5.2}_{-3.1}$	$28.5^{+8.9}_{-8.9}$	$34.7^{+15.7}_{-9.4}$
NGC 4388	$3.3^{+0.5}_{-0.4}$	$1.0^{+0.4}_{-0.2}$	$5.0^{+2.0}_{-1.1}$	$1.3^{+0.1}_{-0.1}$	$0.8^{+0.4}_{-0.2}$	$2.3^{+0.8}_{-0.8}$	$2.3^{+1.1}_{-0.7}$
$N_{\text{PL}}/N_{\text{BMC}} = 24$	$4.1^{+0.7}_{-0.5}$	$1.2^{+0.5}_{-0.3}$	$6.3^{+2.5}_{-1.4}$	$1.6^{+0.2}_{-0.1}$	$1.0^{+0.5}_{-0.3}$	$2.9^{+1.0}_{-1.0}$	$2.9^{+1.4}_{-0.8}$
NGC 4945	$0.5^{+0.06}_{-0.05}$	$0.14^{+0.04}_{-0.03}$	$0.7^{+0.2}_{-0.1}$	$0.2^{+0.01}_{-0.01}$	$0.13^{+0.06}_{-0.04}$	$0.3^{+0.1}_{-0.1}$	$0.4^{+0.2}_{-0.1}$
$N_{\text{PL}}/N_{\text{BMC}} = 24$	$0.6^{+0.1}_{-0.1}$	$0.17^{+0.05}_{-0.03}$	$0.9^{+0.2}_{-0.1}$	$0.3^{+0.02}_{-0.01}$	$0.16^{+0.08}_{-0.05}$	$0.4^{+0.1}_{-0.1}$	$0.5^{+0.2}_{-0.1}$
IC 2560	...	$3.2^{+0.5}_{-0.4}$	$16.1^{+2.0}_{-3.0}$	$10.2^{+1.0}_{-0.5}$	$4.2^{+1.7}_{-1.1}$	$8.4^{+3.0}_{-3.0}$	$12.5^{+5.2}_{-3.2}$
$N_{\text{PL}}/N_{\text{BMC}} = 38$...	$2.8^{+0.4}_{-0.3}$	$14.6^{+1.6}_{-2.0}$	$8.8^{+0.7}_{-0.6}$	$3.6^{+1.5}_{-0.9}$	$7.4^{+2.7}_{-2.7}$	$10.8^{+4.6}_{-2.8}$
Circinus	...	$0.4^{+0.1}_{-0.1}$	$0.5^{+0.2}_{-0.1}$	$0.4^{+0.1}_{-0.1}$	$1.6^{+0.6}_{-0.4}$
$N_{\text{PL}}/N_{\text{BMC}} = 38$...	$0.3^{+0.1}_{-0.1}$	$0.4^{+0.2}_{-0.1}$	$0.6^{+0.4}_{-0.4}$	$1.2^{+0.5}_{-0.3}$

Columns: 1 = AGN name. 2–8 = black hole masses determined with the X-ray scaling method. Subscripts denote GROD05 = reference source GRO J1655-40 in the decreasing phase; GROR05 = reference source GRO J1655-40 in the rising phase; GXD03 = reference source GX 339-4 in the decreasing phase; GXR03 = reference source GX 339-4 in the rising phase; XTER98 = reference source XTE J1550-564 in the rising phase; 3*XTER98 = reference source XTE J1550-564 in the rising phase with a multiplicative correction of a factor 3 applied. Note, the average value (in column 7) is obtained averaging all the M_{BH} obtained from all the reference sources but excluding 3*XTER98. Note: For each source the first line reports the M_{BH} values obtained using $N_{\text{PL}}/N_{\text{BMC}} = 30$ in the spectral fitting; the second line (present only for sources with relatively flat or steep spectra) explicitly states the different value of $N_{\text{PL}}/N_{\text{BMC}}$ used.

host galaxy. The most reliable ways to determine the M_{BH} are direct dynamical methods, which measure the orbital parameters of “test particles”, whose motion is dominated by the gravitational force of the supermassive BH. For example, the mass of the supermassive BH at the center of our Galaxy has been tightly constrained by detailed studies of the orbits of a few innermost stars observed over several years (e.g., [Ghez et al. 2008](#); [Gillessen et al. 2009](#)). In nearby weakly active galaxies, the M_{BH} is determined by the gas dynamics within the sphere of influence of the BH (e.g., [Gebhardt et al. 2003](#)). On the other hand, in bright type 1 AGN, the M_{BH} measurement is obtained from the dynamics of the BLR via the reverberation mapping technique (e.g., [Peterson et al. 2004](#)). Finally, in heavily absorbed type 2 AGN, where the BLR is completely obscured, the only possible direct measurement of the M_{BH} is based on megamaser measurements (e.g., [Kuo et al. 2011](#) and references therein).

The main problem with direct dynamical methods is that they are fairly limited in their application. For instance, direct measurements of M_{BH} via gas dynamics are limited to nearby weakly active galaxies, where the sphere of influence is not outshined by the AGN and are sufficiently close to be resolvable at the angular resolution of ground-based observatories. Similarly, the reverberation mapping technique, which is heavily time and instrument consuming, is limited to type 1 AGN with small or moderate masses. Finally, the megamaser emission in type 2 AGN is relatively rare, and only when the megamaser originates in the accretion disk (as opposed to the jet and outflows)

can this technique be used to constrain the M_{BH} (e.g., [Panessa et al. 2020](#) and references therein).

Fortunately, there are a few robust indirect methods that make it possible to constrain the M_{BH} beyond the range of applicability of the direct dynamical ones. For example, the tight correlation between M_{BH} and the stellar velocity dispersion in the bulge σ_* , observed in nearby nearly quiescent galaxies (e.g., [Tremaine et al. 2002](#)), can be extrapolated to constrain the M_{BH} in many distant and more active galaxies. Similarly, the empirical relationship between the BLR radius and optical luminosity makes it possible to determine the mass of numerous type 1 AGN with only one spectral measurement without the need of long monitoring campaigns (e.g., [Kaspi et al. 2000](#)).

Although indirect methods have proven to be very useful to derive general results for large samples of AGN, caution must be applied when these methods are extrapolated well beyond the original range of applicability of the direct methods. To check for consistency and avoid potential biases associated with the various assumptions inherent in these indirect methods, it is important to develop and utilize alternative techniques to constrain the M_{BH} . In this perspective, X-ray-based methods may offer a useful complementary way to the more commonly used optically based ones, since X-rays that are produced very close to the BH are less affected by absorption and by star and galaxy contamination. Indeed, model-independent methods based on X-ray variability yielded M_{BH} values broadly consistent with those

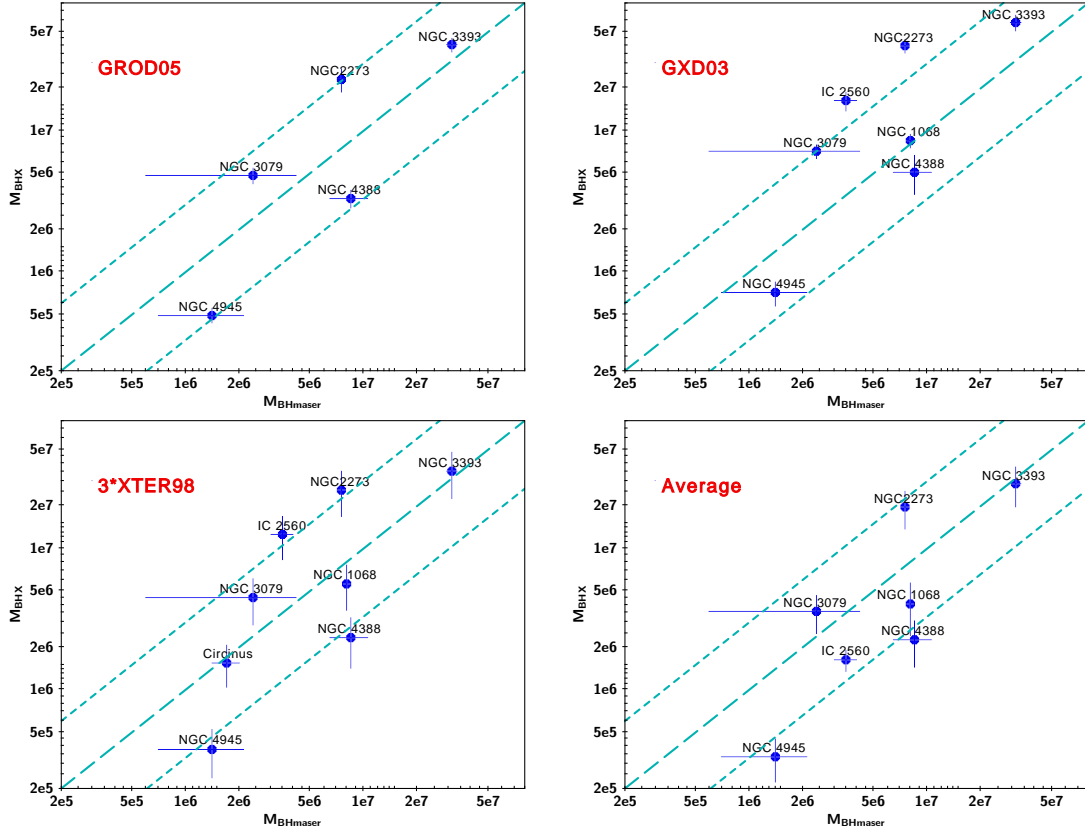


Figure 6. $M_{\text{BH},X}$, the BH mass obtained with the scaling method plotted versus $M_{\text{BH},\text{maser}}$ obtained from the megamaser. The top left panel shows the X-ray scaling values derived from the GROD05 reference, the top right panel those from GXD03, the bottom left the values from 3*XTER98, and the bottom right panel the M_{BH} values obtained from the average of all the available reference sources. The longer-dashed line represents the perfect one-to-one correspondence between the two methods, i.e., a ratio $M_{\text{BH},\text{maser}}/M_{\text{BH},X} = 1$, whereas the shorter-dashed lines indicate the ratios of 3 and 1/3, respectively.

obtained with dynamical methods (e.g. Papadakis 2004; Nikolaćuk et al. 2006; McHardy et al. 2006; Ponti et al. 2012). In a previous work focused on a sample of AGN with reverberation mapping measurements and good quality *XMM-Newton* data, we demonstrated that the X-ray scaling method also provides results in agreement with reverberation mapping within the respective uncertainties (Gliozzi et al. 2011).

It is important to bear in mind that the X-ray scaling method is not equivalent to making some general assumptions on the accretion rate and the bolometric correction and deriving the BH mass from the X-ray luminosity using the formula $M_{\text{BH}} = \kappa_{\text{bol}} L_X / (1.3 \times 10^{38} \lambda_{\text{Edd}})$, where κ_{bol} is the bolometric correction that may range from 15 to 150 depending on the accretion rate of the source (Vasudevan & Fabian 2009), and L_X the X-ray luminosity in erg/s. With this simple equation, without an a priori knowledge of the accretion rate of the source, one could at best obtain the order of magnitude of the M_{BH} . Since λ_{Edd} can vary over a broad range (for example, for this small sample of obscured AGN, the Eddington ratio varies from 0.01 to 0.3), it is not possible to obtain a specific value of M_{BH} that can be quantitatively compared with the value obtained from the dynamical method and find a good agreement, as we did with the scaling method.

One may then argue that the only important parameter in the scaling method is N_{BMC} (because of its direct dependence on the accretion luminosity and distance) and that it is still possible to obtain a good agreement with the dynamically estimated M_{BH} with any value of the photon index. To test this hypothesis, we have selected the two sources with the flattest spectra of our sample (NGC 4388

and NGC 4945) and the two sources with the steepest spectra (IC 2560 and Circinus), and recalculated their M_{BH} with the scaling method assuming $\Gamma = 2.17$ for the flattest sources and $\Gamma = 1.66$ for the steepest sources. This led to changes of M_{BH} by a factor slightly larger than 2 (note that considerably larger changes of M_{BH} would have resulted if we had used a larger difference in the photon indices instead of the minimum and maximum values of this small sample). If the photon index did not play any role, then these M_{BH} changes should have not made a difference in the agreement with the values obtained via the dynamical method, with some objects showing a slightly better agreement and others a slightly worse agreement. Instead, all four sources, which were originally consistent with their maser respective estimates based on the mass ratio criterion described above (see Table 5 and Figure 6), showed a clear departure from the dynamical M_{BH} values with three sources (NGC 4388, NGC 4945, and IC 2560) that were not formally consistent with the maser values anymore (their new mass ratios were 8.0, 7.1, and 6.7, respectively) and only Circinus (ratio of 0.5) still consistent, but only by virtue of the fact that the original ratio was basically 1. We therefore conclude that the scaling method works because the photon index accurately characterizes the accretion state of accreting black holes and allows the correct selection of the reference source's N_{BMC} value to be compared with the AGN's value.

In this study, we have extended the X-ray scaling method to a sample of heavily obscured type 2 AGN with M_{BH} already constrained by megamaser measurements. This dynamical method is rightly considered one of the most reliable; however, the accuracy of the M_{BH}

Table 4. $\Delta M_{\text{BH}}/\sigma_{\text{diff}}$: Comparison between M_{BH} from maser and X-ray scaling

Source name (1)	$\Delta M_{\text{BH}}/\sigma$						
	GROD05 (2)	GROR05 (3)	GXD03 (4)	GXR04 (5)	XTER98 (6)	average (7)	3*XTER98 (8)
NGC 1068	...	16.7	−0.5	10	8.6	2.5	1.2
NGC 1194	19.0	20.5	11.3	21.0	21.0	18.3	20.4
$N_{\text{PL}}/N_{\text{BMC}}=24$	17.9	19.7	6.0	20.8	20.8	16.7	20.0
NGC 2273	−3.5	0.1	−7.3	−9.7	−0.4	−2.0	−2.0
NGC 3079	−1.2	0.6	−2.4	−0.4	0.5	−0.6	−0.9
NGC 3393	−1.8	7.3	−3.4	3.2	4.2	0.3	−0.3
NGC 4388	2.5	3.7	1.4	3.6	3.8	2.9	2.8
$N_{\text{PL}}/N_{\text{BMC}}=24$	2.1	3.6	0.8	3.4	3.7	2.5	2.4
NGC 4945	1.3	1.8	1.0	1.7	1.8	1.5	1.4
$N_{\text{PL}}/N_{\text{BMC}}=24$	1.1	1.8	0.6	1.6	1.8	1.4	1.3
IC 2560	...	0.5	−4.9	−7.5	−0.4	−1.6	−2.1
$N_{\text{PL}}/N_{\text{BMC}}=38$...	1.1	−5.7	−6.3	−0.1	−1.4	−2.0
Circinus	...	4.4	3.4	4.1	0.3
$N_{\text{PL}}/N_{\text{BMC}}=38$...	4.7	4.0	2.3	1.0

Columns: 1 = AGN name. 2–8 = Change in black hole mass over error for each reference source. Reference sources: GROD05 = reference source GRO J1655-40 in the decreasing phase; GROR05 = reference source GRO J1655-40 in the rising phase; GXD03 = reference source GX 339-4 in the decreasing phase; GXR03 = reference source GX 339-4 in the rising phase; XTER98 = reference source XTE J1550-564 in the rising phase; 3*XTER98 = reference source XTE J1550-564 in the rising phase with a multiplicative correction of a factor 3 applied. Note, the average value (in column 7) is obtained averaging all the M_{BH} obtained from all the reference sources but excluding 3*XTER98. Note: For each source the first line reports the values obtained using $N_{\text{PL}}/N_{\text{BMC}} = 30$ in the spectral fitting; the second line (present only for sources with relatively flat or steep spectra) explicitly states the different value of $N_{\text{PL}}/N_{\text{BMC}}$ used.

derived with this technique depends on the quality of the radio data, on the assumption that the megamaser emission is produced in an edge-on disk, and that its rotation curve is strictly Keplerian. Additionally, one should bear in mind that this technique measures the mass enclosed within the megamaser emission. As a consequence, the actual M_{BH} may be slightly smaller if the measured enclosed mass encompasses a nuclear cluster or the inner part of a massive disk, or alternatively slightly larger if radiation pressure (not included in the M_{BH} derivation) plays an important role (Kuo et al. 2011).

Specifically, for the sources of our sample, the rotation curve traced by the megamaser in NGC 1068 is non-Keplerian; the M_{BH} was derived assuming a self-gravitating accretion disk model (Lodato & Bertin 2003). NGC 1194 displays one of the largest maser disks (with inner and outer radii of 0.54 and 1.33 parsecs) which appears to be slightly bent and is consistent with Keplerian rotation (Kuo et al. 2011). NGC 2273 also shows indications of a warped but much smaller disk (with inner and outer disk radii of 0.028 and 0.084 pc) with Keplerian rotation (Kuo et al. 2011). In NGC 3079 the disk appears to be thick and flared (Kondratko, Greenhill, & Moran 2005), whereas in NGC 3393 the maser seems to describe a flat disk perpendicular to the kpc radio jet, and the positions of the maser points have substantial uncertainties (Kondratko, Greenhill, & Moran 2008). NGC 4388, located in the Virgo cluster, has only five megamaser spots, which make it impossible to demonstrate that they lie on a disk or that the rotation is Keplerian (Kuo et al. 2011). For this reason, to reflect the actual uncertainty on the M_{BH} derived by

megamaser measurements, we have increased the statistical error by a factor of 10, leading to an uncertainty of $\sim 24\%$. The megamaser in NGC 4945 has been modeled as an edge-on thin disk, although this is not the only possible interpretation of the data; the non-Keplerian rotation of the blue-shifted emission and the substantial position errors lead to a relatively large uncertainty in the M_{BH} of $\sim 50\%$ (Greenhill et al. 1997). In IC 2560 the megamaser emission has been attributed to an edge-on thin disk with Keplerian rotation with some additional contribution from a jet (Yamauchi et al. 2012). Finally, the megamaser emission in Circinus appears to be associated with a warped accretion disk and a wide-angle outflow (Greenhill et al. 2003). In summary, because of the presence of outflows, jets, disk warps, or non-Keplerian rotation curves, we should consider the M_{BH} values determined from megamaser measurements as robust estimates but not as extremely accurate values, and the errors reported in Table 1 are likely lower limits on their actual uncertainties.

With respect to type 1 AGN, the main difficulty of applying the X-ray scaling method to heavily obscured AGN is the need to properly constrain the parameters of the primary emission in sources whose X-ray spectra are dominated by absorption and reflection. However, the *NuSTAR* spectra of these specific sources, often complemented with *Chandra* and *XMM-Newton* data, were the object of very detailed analyses, which led to the disentanglement and a careful characterization of the different contributions of the AGN direct and reprocessed emission, of the host galaxy, and of the off-nuclear sources located in the spectral extraction region (e.g., Yaqoob

Table 5. Ratio between M_{BH} values obtained from maser measurements and the X-ray scaling method: $M_{\text{BH,maser}}/M_{\text{BH,scaling}}$

Source name (1)	Ratio						
	GROD05 (2)	GROR05 (3)	GXD03 (4)	GXR04 (5)	XTER98 (6)	average (7)	3*XTER98 (8)
NGC 1068	...	5.1 ± 0.8	0.9 ± 0.1	1.9 ± 0.1	4.3 ± 1.5	2.0 ± 0.8	1.4 ± 0.5
NGC 1194	12 ± 2	38 ± 16	7 ± 3	32 ± 3	52 ± 21	17 ± 7	17 ± 7
$N_{\text{PL}}/N_{\text{BMC}} = 24$	10 ± 2	30 ± 15	6 ± 4	27 ± 3	44 ± 18	13 ± 6	15 ± 6
NGC 2273	0.3 ± 0.1	1.0 ± 0.2	0.20 ± 0.02	0.40 ± 0.03	0.9 ± 0.3	0.4 ± 0.1	0.3 ± 0.1
NGC 3079	0.5 ± 0.4	1.8 ± 1.4	0.3 ± 0.3	0.8 ± 0.6	1.6 ± 1.3	0.7 ± 0.5	0.5 ± 0.4
NGC 3393	0.8 ± 0.1	2.9 ± 0.6	0.5 ± 0.1	1.3 ± 0.1	2.7 ± 1.0	1.1 ± 0.3	0.9 ± 0.3
NGC 4388	2.6 ± 0.7	8.8 ± 3.6	1.7 ± 0.7	6.5 ± 1.6	10.9 ± 5.0	3.7 ± 1.6	3.6 ± 1.7
$N_{\text{PL}}/N_{\text{BMC}} = 24$	2.1 ± 0.6	7.0 ± 2.8	1.3 ± 0.5	5.2 ± 1.3	8.7 ± 4.0	3.0 ± 1.3	2.9 ± 1.3
NGC 4945	2.8 ± 1.5	10.3 ± 5.7	2.0 ± 1.1	6.2 ± 3.1	11 ± 6.9	4.1 ± 2.5	3.7 ± 2.3
$N_{\text{PL}}/N_{\text{BMC}} = 24$	2.3 ± 1.2	8.2 ± 4.6	1.6 ± 1.2	4.8 ± 2.4	8.7 ± 5.4	3.3 ± 2.0	2.9 ± 1.8
IC 2560	...	1.1 ± 0.2	0.2 ± 0.1	0.3 ± 0.1	0.8 ± 0.3	0.4 ± 0.2	0.3 ± 0.1
$N_{\text{PL}}/N_{\text{BMC}} = 38$...	1.3 ± 0.2	0.2 ± 0.1	0.4 ± 0.1	1.0 ± 0.4	0.5 ± 0.2	0.3 ± 0.1
Circinus	...	4.6 ± 0.8	3.3 ± 1.2	3.9 ± 0.9	1.1 ± 0.4
$N_{\text{PL}}/N_{\text{BMC}} = 38$...	5.9 ± 1.3	4.3 ± 1.6	2.7 ± 1.6	1.4 ± 0.5

Columns: 1 = AGN name. 2–8 = Ratio of maser to X-ray scaling for each reference source. Reference sources: GROD05 = reference source GRO J1655-40 in the decreasing phase; GROR05 = reference source GRO J1655-40 in the rising phase; GXD03 = reference source GX 339-4 in the decreasing phase; GXR03 = reference source GX 339-4 in the rising phase; XTER98 = reference source XTE J1550-564 in the rising phase; 3*XTER98 = reference source XTE J1550-564 in the rising phase with a multiplicative correction of a factor 3 applied. Note, the average value (in column 7) is obtained averaging all the M_{BH} obtained from all the reference sources but excluding 3*XTER98. Note: For each source the first line reports the values obtained using $N_{\text{PL}}/N_{\text{BMC}} = 30$ in the spectral fitting; the second line (present only for sources with relatively flat or steep spectra) explicitly states the different value of $N_{\text{PL}}/N_{\text{BMC}}$ used.

2012; Puccetti et al. 2014; Arévalo et al. 2014; Bauer et al. 2015). Guided by these findings, we were able to parametrize the torus contribution using the physically motivated self-consistent model Borus (Baloković et al. 2018) instead of the MYTorus or Torus models used in the previous analyses. To characterize the primary emission, instead of the phenomenological power-law model, we utilized the BMC Comptonization model, since the scaling method directly scales the normalization of this model N_{BMC} between AGN and an appropriate stellar reference to determine M_{BH} .

With our baseline spectral model, where we assumed $N_{\text{PL}}/N_{\text{BMC}} = 30$, as described in detail in Section 3 (see also the Appendix for details on the spectral fittings of individual sources), and applying the scaling technique summarized in Section 4.1, we obtained the following results:

- Many of the M_{BH} values, obtained with different reference trends, are broadly in agreement with the corresponding megamaser ones. In particular, the estimates derived using GROD05, 3*XTER98, and the ones obtained by averaging the values inferred from all the available reference sources, are consistent at the 3σ level, based on measurements of $\Delta M_{\text{BH}}/\sigma_{\text{diff}} = (M_{\text{BH,maser}} - M_{\text{BH,scaling}})/\sigma_{\text{diff}}$, which are reported in Table 4 and shown in Fig. 5.
- The agreement between the two methods is confirmed by the $M_{\text{BH,maser}}/M_{\text{BH,scaling}}$ ratio: for all type 2 AGN of our sample $(M_{\text{BH,maser}}/M_{\text{BH,scaling}}) \pm 3\sigma \leq 1$, when using the best reference sources or the average M_{BH} , as summarized in Table 5. Fig. 6 illus-

trates the good agreement between the two methods, showing that GROD05, GXD04 (partially), 3*XTER98, and the average obtained from all reference patterns are all consistent with the one-to-one ratio within a factor of three.

- The only object of our sample for which the M_{BH} inferred from the X-ray scaling method is statistically inconsistent with the megamaser value is NGC 1194, which is the AGN with the lowest accretion rate ($\lambda_{\text{Edd}} \approx 7 \times 10^{-3}$). However, this discrepancy is expected, since the X-ray scaling method cannot be applied in this regime, where Γ generally shows an anti-correlation with λ_{Edd} .

In conclusion, our work demonstrates that the same X-ray scaling method works equally well for type 1 AGN (given the formal agreement with the reverberation mapping sample) and type 2 AGN (based on the agreement with the megamaser sample). We thus conclude that this method can be safely applied to any type of AGN regardless of their level of obscuration, provided that these sources accrete above a minimum threshold and that their primary X-ray emission can be robustly characterized via spectral analysis. This also proves that this method is robust and can be used to complement the various indirect methods, especially when they are applied well beyond the range of validity of the direct methods, from which they were calibrated. Finally, the X-ray scaling method offers the possibility to investigate in a systematic and homogeneous way the existence of any intrinsic difference in the fundamental properties of the central engines in type

1 and type 2 AGN. We plan to carry out this type of investigation in our future work.

ACKNOWLEDGEMENTS

We thank the anonymous referee for constructive comments and suggestions that improved the clarity of the paper and helped strengthen our conclusions. This research has made use of data, software, and/or web tools obtained from the High Energy Astrophysics Science Archive Research Center (HEASARC), a service of the Astrophysics Science Division at NASA/GSFC and of the Smithsonian Astrophysical Observatory's High Energy Astrophysics Division, and of the NuSTAR Data Analysis Software (NuSTARDAS) jointly developed by the ASI Science Data Center (ASDC, Italy) and the California Institute of Technology (Caltech, USA).

DATA AVAILABILITY

The data underlying this article are available in the High Energy Astrophysics Science Archive Research Center (HEASARC) Archive at <https://heasarc.gsfc.nasa.gov/docs/archive.html>.

REFERENCES

- Antonucci R. R. J., 1983, *Nature*, 303, 158
 Antonucci R. R. J., 1993, *ARA&A*, 31, 473
 Arévalo P. et al., 2014, *ApJ*, 791, 81
 Arnaud K. A., 1996, *ASPC*, 101, 17
 Baloković M. et al., 2018, *ApJ*, 854, 42
 Bauer F. E. et al., 2015, *ApJ*, 812, 116
 Blandford R. D., McKee C. F., 1982, *ApJ*, 255, 419
 Brightman M. et al., 2013, *MNRAS*, 433, 2485
 Brightman M. et al., 2016, *ApJ*, 826, 93
 Brightman M., Nandra K., 2011, *MNRAS*, 413, 1206
 Constantin A., Green P., Aldcroft T., Kim D.-W., Haggard D., Barkhouse W., Anderson S. F., 2009, *ApJ*, 705, 1336
 Gebhardt K. et al., 2003, *ApJ*, 583, 92
 Ghez A. M. et al., 2008, *ApJ*, 689, 1044
 Giacché S., Gilli R., Titarchuk L., 2014, *A&A*, 562A, 44
 Gillessen S., Eisenhauer F., Trippe S., Alexander T., Genzel R., Martins F., Ott T., 2009, *ApJ*, 692, 1075
 Gliozzi M., Papadakis I. E., Grupe D., Raeth C., Kedziora-Chudczer L., 2010, *ApJ*, 717, 1243
 Gliozzi M., Titarchuk L., Satyapal S., Price D., Jang I., 2011, *ApJ*, 735, 16
 Gliozzi M., Williams J. K., 2020, *MNRAS*, 491, 532
 Greenhill L. J., Ellingsen S. P., Norris R. P., Gough R. G., Sinclair M. W., Moran J. M., Mushotzky R., 1997, *ApJL*, 474, L103
 Greenhill L. J. et al., 2003, *ApJ*, 590, 162
 Gu M., Cao X., 2009, *MNRAS*, 399, 349
 Gültekin K., Cackett E. M., Miller J. M., Di Matteo T., Markoff S., Richstone D. O., 2012, *ApJ*, 749, 129
 Hickox R. C., Alexander D. M., 2018, *ARA&A*, 56, 1
 Jang I., Gliozzi M., Hughes C., Titarchuk L., 2014, *MNRAS*, 443, 72
 Jang I., Gliozzi M., Satyapal S., Titarchuk L., 2018, *MNRAS*, 473, 136
 Kaspi S., Smith P. S., Netzer H., Maoz D., Jannuzi B. T., Giveon U., 2000, *ApJ*, 533, 631
 Khachikian E. Y., Weedman D. W., 1974, *ApJ*, 192, 581
 Kondratko P. T., Greenhill L. J., Moran J. M., 2005, *ApJ*, 618, 618
 Kondratko P. T., Greenhill L. J., Moran J. M., 2008, *ApJ*, 678, 87
 Koss M. J. et al., 2015, *ApJ*, 807, 149
 Kuo C. Y. et al., 2011, *ApJ*, 727, 20
 Lodato G., Bertin G., 2003, *A&A*, 398, 517
 Masini A. et al., 2016, *A&A*, 589, A59
 McHardy I. M., Koerding E., Knigge C., Uttley P., Fender R. P., 2006, *Nature*, 444, 730
 Murphy K. D., Yaqoob T., 2009, *MNRAS*, 397, 1549
 Netzer H., 2015, *ARA&A*, 53, 365
 Nikolaćuk M., Czerny B., Ziółkowski J., Gierliński M., 2006, *MNRAS*, 370, 1534
 Osterbrock D. E., 1978, *PNAS*, 75, 540
 Panessa F., Castangia P., Malizia A., Bassani L., Tarchi A., Bazzano A., Ubertini P., 2020, *A&A*, in press, preprint (arXiv:2006.08280)
 Papadakis I. E., 2004, *MNRAS*, 348, 207
 Peterson B. M. et al., 2004, *ApJ*, 613, 682
 Ponti G., Papadakis I., Bianchi S., Guainazzi M., Matt G., Uttley P., Bonilla N. F., 2012, *A&A*, 542, A83
 Puccetti S. et al., 2014, *ApJ*, 793, 26
 Ramos Almeida C., Ricci C., 2017, *Nature Astronomy*, 1, 679
 Remillard R. A., McClintock J. E., 2006, *ARA&A*, 44, 49
 Risaliti G., Young M., Elvis M., 2009, *ApJL*, 700, L6
 Seifina E., Titarchuk L., Shaposhnikov N., 2014, *ApJ*, 789, 57
 Seifina E., Chekhtman A., Titarchuk L., 2018, *A&A*, 613A, 48
 Shaposhnikov N., Titarchuk L., 2009, *ApJ*, 699, 453
 Shemmer O., Brandt W. N., Netzer H., Maiolino R., Kaspi S., 2008, *ApJ*, 682, 81
 Sobolewska M. A., Papadakis I. E., 2009, *MNRAS*, 399, 1597
 Tadhunter C., 2008, *NewAR*, 52, 227
 Titarchuk L., Mastichiadis A., Kylafis N. D., 1997, *ApJ*, 487, 834
 Titarchuk L., Seifina E., 2016a, *A&A*, 585A, 94
 Titarchuk L., Seifina E., 2016b, *A&A*, 595A, 101
 Tremaine S. et al., 2002, *ApJ*, 574, 740
 Urry C. M., Padovani P., 1995, *PASP*, 107, 803
 Vasudevan R. V., Fabian A. C., 2009, *MNRAS*, 392, 1124
 Williams J. K., Gliozzi M., Rudzinsky R. V., 2018, *MNRAS*, 480, 96
 Yamauchi A., Nakai N., Ishihara Y., Diamond P., Sato N., 2012, *PASJ*, 64, 103
 Yaqoob T., 2012, *MNRAS*, 423, 3360

APPENDIX A: ADDITIONAL SPECTRAL RESULTS

NGC 1068: A detailed analysis of the *NuSTAR*, *XMM-Newton*, and *Chandra* spectra of this source was carried out by [Bauer et al. \(2015\)](#). Thanks to the excellent sensitivities of *XMM-Newton* and *NuSTAR* over broad complementary energy ranges, and to the sub-arcsecond spatial resolution of *Chandra*, the authors were able to disentangle the contributions of the host galaxy and off-nuclear sources from the AGN emission within the *NuSTAR* extraction region. The overall best-fit model is fairly complex and comprises several Fe and Ni emission lines, a Bremsstrahlung component to account for the radiative recombination continuum and lines, a cutoff power-law model to account for the off-nuclear X-ray sources, in addition to the AGN-related emission, which is parametrized by two different MYTorus scattered and line components, in addition to the transmitted one described by the zeroth-order component of that model. In our fitting, in addition to our baseline model we added the Bremsstrahlung and cutoff power law with all parameters fixed at the values provided by [Bauer et al. \(2015\)](#), and a Gaussian line to roughly model the excess around 6.5 keV. To account for the multiple absorption components, we also added a second Borus model, whose best-fit parameters are $\log(N_{\text{H,por}}) = 24.9 \pm 0.1$, $\text{CFtor} = 83\%$, and $A_{\text{Fe}} = 1$. Our best-fit parameters are broadly consistent with the results presented by [Bauer et al. \(2015\)](#). The observed flux in the 2–10 keV energy band is $5.4 \times 10^{-12} \text{ erg cm}^{-2} \text{ s}^{-1}$, and the intrinsic one (i.e., corrected for absorption) $1.3 \times 10^{-10} \text{ erg cm}^{-2} \text{ s}^{-1}$.

NGC 1194: The starting model for the spectral fit of this source is provided by the work of [Masini et al. \(2016\)](#), who fitted the *NuSTAR* spectrum with the MYTorus model in the decoupled mode,

with the addition of a Gaussian line at 6.8 keV, and a scattering fraction of the primary continuum of $f_s \sim 3\%$. In our fitting, we used our baseline model and found the main parameters (Γ , N_H , and f_s) to be fully consistent with their best-fit results. The 2–10 keV observed flux is 1.2×10^{-12} erg cm $^{-2}$ s $^{-1}$, and the intrinsic one 1.0×10^{-11} erg cm $^{-2}$ s $^{-1}$.

NGC 2273: The starting spectral model for this source is again provided by the work of [Masini et al. \(2016\)](#), who fitted the *NuSTAR* spectrum with the *Torus* model that favored a heavily absorbed scenario with $N_H > 7 \times 10^{24}$ cm $^{-2}$. In our fitting, we used our baseline model, which yielded a best fit broadly consistent with their results. The 2–10 keV observed flux is 9.2×10^{-13} erg cm $^{-2}$ s $^{-1}$, and the intrinsic one 3.6×10^{-10} erg cm $^{-2}$ s $^{-1}$.

NGC 3079: The starting spectral model for this source is again provided by the work of [Masini et al. \(2016\)](#), who fitted the *NuSTAR* spectrum with the *MYTorus* model in a coupled mode. The results obtained with our baseline model are consistent within the respective uncertainties with their results. The 2–10 keV observed flux is 6.4×10^{-13} erg cm $^{-2}$ s $^{-1}$, and the intrinsic one 1.2×10^{-10} erg cm $^{-2}$ s $^{-1}$.

NGC 3393: The starting spectral model for this source is provided by the work of [Koss et al. \(2015\)](#) and [Masini et al. \(2016\)](#), who fitted the *NuSTAR* spectrum with both *MYTorus* and *Torus* models. The results obtained with our baseline model are broadly consistent with the results presented by these authors with a slightly larger value of N_H (10^{25} vs. 2.2×10^{24} cm $^{-2}$). The 2–10 keV observed flux is 4.4×10^{-13} erg cm $^{-2}$ s $^{-1}$, and the intrinsic one 8.3×10^{-11} erg cm $^{-2}$ s $^{-1}$.

NGC 4388: The starting spectral model for this source is once more provided by the work of [Masini et al. \(2016\)](#), who fitted the *NuSTAR* spectrum with the *MYTorus* and *Torus* models, which favor a Compton-thin scenario with a substantial scattered primary emission that dominates below 5 keV. The results from our baseline model are fully consistent with their results. The 2–10 keV observed flux is 7.9×10^{-12} erg cm $^{-2}$ s $^{-1}$, and the intrinsic one 1.4×10^{-11} erg cm $^{-2}$ s $^{-1}$.

NGC 4945: A detailed analysis of the *NuSTAR*, *Suzaku*, and *Chandra* spectra of this source was carried out by [Puccetti et al. \(2014\)](#), who in turn, were guided by the results obtained by [Yaqoob \(2012\)](#) based on a comprehensive analysis of all the hard X-ray spectra available at that time. The wealth of high-quality broad-band spectra obtained with several observatories made it possible to parametrize separately the different contributions of the host galaxy, the AGN, and contaminating sources within the *NuSTAR* extraction region. The best-fit model is fairly complex and comprises several emission lines, the galaxy optically thin thermal continuum, which is described by the APEC model, the contamination from off-nuclear sources parametrized by a power law, and the AGN emission seen through a torus described by the *MYTorus* model in the decoupled mode. In our fitting procedure, in addition to our baseline model we included the APEC and power-law models with all parameters fixed at the values provided by Yaqoob. Our results are broadly consistent with those obtained by both Yaqoob and Puccetti. The 2–10 keV observed flux is 3.7×10^{-12} erg cm $^{-2}$ s $^{-1}$, and the intrinsic one 2.7×10^{-10} erg cm $^{-2}$ s $^{-1}$.

IC 2560: The starting spectral model for this source is again provided by the work of [Masini et al. \(2016\)](#), who fitted the *NuSTAR* spectrum with the *Torus* model, which favors a heavily absorbed primary emission characterized by a steep photon index. The results from our baseline model are broadly consistent with their results. The 2–10 keV observed flux is 3.7×10^{-13} erg cm $^{-2}$ s $^{-1}$, and the intrinsic one 1.7×10^{-10} erg cm $^{-2}$ s $^{-1}$.

Circinus: A detailed analysis of the *NuSTAR*, *XMM-Newton*, and *Chandra* spectra of this source was carried out by [Arévalo et al.](#)

(2014). Combining the complementary properties of these observatories (i.e., the high sensitivities of *XMM-Newton* and *NuSTAR* over broad energy ranges and the sub-arcsecond spatial resolution of *Chandra*), the authors were able to disentangle the contributions of different contamination sources (diffuse emission from the host galaxy, supernova remnant contribution, and off-nuclear X-ray binary sources) from the AGN emission within the *NuSTAR* extraction region. The overall best-fit model is complex and comprises several emission lines, an APEC model for the diffuse emission, three *Mekal* models to parametrize the supernova remnant, and a power-law model to account for the off-nuclear point-like sources, in addition to two different *MYTorus* models used in the decoupled mode. In our fitting, in addition to our baseline model we added all the contamination models with all the parameters fixed at the values provided by [Arévalo et al. \(2014\)](#) and three Gaussian lines to roughly model the line excess in the 5.5–7.5 keV range. To account for the multiple absorption components, we also added a second *Borus* model, whose best-fit parameters are $\log(N_{H_{\text{bor}}}) = 24.6 \pm 0.1$, $\text{CFtor} = 10\%$, and $A_{\text{Fe}} = 1$. Our best-fit parameters are broadly consistent with their results. The 2–10 keV observed flux is 2.0×10^{-11} erg cm $^{-2}$ s $^{-1}$, and the intrinsic one 2.1×10^{-10} erg cm $^{-2}$ s $^{-1}$.

APPENDIX B: THE X-RAY SCALING METHOD

The X-ray scaling method for determining the mass of a black hole (M_{BH}) was first described by [Shaposhnikov & Titarchuk \(2009\)](#) and first applied to AGN by [Glozzi et al. \(2011\)](#), where the method is described in detail. Here, we only report the essential information on the stellar reference sources – their M_{BH} values and distances (Table B1) and the mathematical expression of the spectral trend with the best fit parameters for the different sources (Table B2) – that is needed to reproduce the M_{BH} values. The two steps below accomplish the scaling described in Section 4.1.

Step 1. Use the following equation to solve for $N_{\text{BMC},r}$, the BMC normalization the reference source would have at the same photon index as the target AGN. The reference source is a Galactic, stellar-mass black hole with known mass and distance.

$$N_{\text{BMC},r}(\Gamma) = N_{\text{tr}} \times \left\{ 1 - \ln \left[\exp \left(\frac{A - \Gamma}{B} \right) - 1 \right] \right\}^{(1/\beta)} \quad (\text{B1})$$

where Γ is the photon index of the target AGN as determined by the spectral fit, and A , B , N_{tr} , and β are given in Table B2. Note: this equation was first presented by [Jang et al. \(2018\)](#) with an error: there should be a minus sign before the logarithm.

Step 2. Use the equation presented in Section 4.1 to solve for $M_{\text{BH},t}$.

$$M_{\text{BH},t} = M_{\text{BH},r} \times \left(\frac{N_{\text{BMC},t}}{N_{\text{BMC},r}} \right) \times \left(\frac{d_t}{d_r} \right)^2 \quad (\text{B2})$$

where M_{BH} is the black hole mass, N_{BMC} is the BMC normalization, and d is the distance. The t subscript denotes the target AGN and the r subscript denotes the reference source.

This paper has been typeset from a \LaTeX file prepared by the author.

Table B1. Characteristics of reference sources

Name	M_{BH} (M_{\odot})	d (kpc)
GRO J1655-40	6.3 ± 0.3	3.2 ± 0.2
GX 339-4	12.3 ± 1.4	5.7 ± 0.8
XTE J1550-564	10.7 ± 1.5	3.3 ± 0.5

 Source: [Gliozzi et al. \(2011\)](#)
Table B2. Parametrization of Γ - N_{BMC} reference patterns

Transition (1)	A (2)	B (3)	N_{tr} (4)	β (5)
GRO J1655-40 D05	1.96 ± 0.02	0.42 ± 0.02	0.023 ± 0.001	1.8 ± 0.2
GRO J1655-40 R05	2.35 ± 0.04	0.74 ± 0.04	0.131 ± 0.001	1.0 ± 0.1
GX 339-4 D03	2.13 ± 0.03	0.50 ± 0.04	0.0130 ± 0.0002	1.5 ± 0.3
GX 339-4 R04	2.10 ± 0.03	0.46 ± 0.01	0.037 ± 0.001	8.0 ± 1.5
XTE J1550-564 R98	2.96 ± 0.02	2.8 ± 0.2	0.055 ± 0.010	0.4 ± 0.1

Columns: 1 = reference source spectral transition. 2 = parameter that determines the rigid translation of the spectral pattern along the y-axis. 3 = parameter characterizing the lower saturation level of the pattern. 4 = parameter that determines the rigid translation of the spectral pattern along the x-axis. 5 = slope of the spectral pattern. Source: [Gliozzi et al. \(2011\)](#)